International Journal of Microwave and Wireless Technologies

cambridge.org/mrf

Machine learning-optimized modified dual staircase-shaped fractal antenna: design and experimental analysis

Manpreet Kaur[1], Navneet Kaur[2] and Jagtar Singh Sivia[1]

[1]Yadavindra Department of Engineering, PUGKC, Talwandi Sabo, PB, India and [2]Electronics and Telecommunication Division, MIE, Institution of Engineers, India

Research Paper

Cite this article: Kaur M, Kaur N, Sivia JS (2026) Machine learning-optimized modified dual staircase-shaped fractal antenna: design and experimental analysis. *International Journal of Microwave and Wireless Technologies* **18**(2), 235–249. https://doi.org/10.1017/S1759078726103122

Received: 25 August 2025
Revised: 4 March 2026
Accepted: 15 March 2026

Keywords:
ANN; fractal; Harmony Search Algorithm; Mean Absolute Error; staircase-shaped

Corresponding author: Manpreet Kaur; Email: sketty@rediffmail.com

Abstract

This research paper proposes an innovative, mathematically engaging, and compact Dual Staircase-Shaped Fractal Antenna (DSSFA) using an HSA-ANN Ensembled integrated approach. The revealed structure bearing size $26 \times 32 \times 1.6$ mm^3 is tailored on an easily accessible FR4 substrate and backed by a modified ground plane. The considered fractal radiator is designed iteratively and exhibits a symmetrical dual staircase-shape. During the generation process, the framed HSA-ANN Ensembled integrated strategy offers the targeted frequency points. The developed heterogeneous ANN Ensembled Models are employed for the prediction of two critical design parameters (feed position and ground length). Afterward, the trained Ensembled models are utilized in the fitness function of the HSA for the creation of optimized operating points. Furthermore, laboratory measurements on the Realized DSSFA are carried out to justify the feasibility of the described fractal approach. The examined resonant points are 2.48, 3.58, 4.25, 7.65, 8.74, 11.83, and 14.44 GHz. At the claimed resonant points, the said antenna is characterized by stable partially deformed omnidirectional/bidirectional radiation patterns. The demonstrated fractalization technique allows the physical size to be reduced by 33%. Based on the experimentation, it has been stated that the introduced antenna is intended for use in distinct wireless applications.

Introduction

Over the last few decades, Wireless Communication (WC) has experienced a rapid boom in the deployment of electronic appliances, and further more development is expected [1]. Effective WC techniques are considered as the driving force for global revolution. This mode of communication has fully transformed the way of living and created a fully connected society [2]. WC domain encompasses a huge variety of WC devices and technologies, engages in digital connectivity, and hence it offers global coverage. The primary goal of this technology is to allow easy transfer of useful information between the endpoints that are not physically connected [3]. Convenient accessibility, mobility, and constant and high-speed connectivity are the desirable characteristics of a modern WC system [4]. In the present times, modern electronic gadgets like mobile phones, laptops, tablets, mixer players, and other electronic products are the expected items that employ this technology [5]. In addition, the rapid expansion of modern wireless technologies and rising demand for fast data communication have prompted the emergence of novel and innovative antenna designs [6]. In this digital age, designing of an antenna with salient features such as compactness, high data rate, and high fidelity for an efficient WC system is a challenging task. Huge progress in modern WC technologies has triggered a new domain of antenna designing, named as Fractal Antennas (FAs) [7]. The ever-growing advancements in antenna electromagnetics have pushed the fractal design approach to an extraordinary level. Implementation of FAs is an onerous task that requires numerous iterations, starting from a general conceptual strategy to the design implementation [8]. B. B. Mandelbrot is a famous French mathematician who firstly framed the word "fractal" [9]. He had conducted huge research, analyzed numerous fragmented and cracked designs/shapes that exhibit self-similarity and scaling features. Fractal geometries are inspired by natural fractal patterns such as snowflakes, ice crystals, pineapples, broccoli, seashells, peacock fins, spiral galaxies, and so on [10, 11]. Fractal design configurations offer electrical length enhancement associated with the patch without increasing the patch area [12]. Hence, instead of employing numerous radiating elements for specific operational bands, a single component radiator can manage multiresonant bands and satisfy the requirements of WC [13]. As a consequence, FAs are considered as the key choice in modern communication systems as they help in achieving better performance characteristics.

Fractal based geometrical designs have been becoming more popular over the past few years. Different fractal configurations exhibiting significant size reduction and multiband behavior

© The Author(s), 2026. Published by Cambridge University Press in association with The European Microwave Association.

are described in [14–16]. A novel pentagonal FA implemented with modified coplanar ground was projected for Ultra WideBand (UWB) applications [17]. The possessed peak gain was 2.2 dB and the claimed results were highly promising. S. Shandal et al. [18] described the theoretical analysis of a sophisticated circular patch resonator designed with fractalization method. The mentioned design gave two operational points (5.7 and 7.9 GHz) and the associated impedance bandwidth was 4.8 GHz. M. G. Siddiqui et al. [19] suggested a modified A-shaped fractaled triangular geometry that shows its functionality for X, Ku, and K band applications. Moreover, the two-iterated configured geometry was scrutinized using cavity model method. The step-by-step evolution procedure of a modified inverted triangular structure was effectively characterized and reported in [20]. Two alphabetic cuts (H-cut and I-cut) embodied FA of volume = 50 × 60 × 1.6 mm^3 was successfully realized for UWB applications [21]. M. Marzouk et al. [22] discussed a new design of area 1020 mm^2. The investigated frequency range was 3.2–7.5 GHz and the peak gain was 6.8 dB. In recent literature, numerous soft computing methodologies have been employed by distinct researchers and antenna designers to find the best analytical solutions for the complex antenna topologies [23]. Depending on the interest, the authors utilized specific optimization techniques in their work. B. S. Dhaliwal et al. [24] constructed a 1.47 mm thick fractal MIMO antenna with an Artificial Neural Network (ANN) approach. Good consistency among software produced and experimentally computed outcomes authenticated the recommended ANN approach. An ANN based small-scaled hybridized fractal design was created and verified experimentally for biomedical applications in [25]. S. Rajapriya et al. [26] illustrated a small-sized Hilbert curve fractal antenna embedded with a rectangular split ring resonator. The important geometric parameters were optimized with the demonstrated ANN approach. In [27], Invasive Weed Optimization based conglomerated fractal antenna was realized and its functional behavior was compared with the same antenna implemented using Harmony Search Algorithm (HSA). Y.A. Mohammed and D.K. Naji [28] effectively applied the concept of HSA in antenna arrays for sidelobe suppression. The usefulness of HSA approach for the optimal pattern synthesis of antenna arrays was illustrated in [29].

This research work is primarily concerned with the implementation and analysis of a HSA-ANN Ensembled integrated approach based modified dual staircase-shaped multiband fractal antenna. Using the developed hybrid algorithm, this meticulously engineered antenna is designed with an aim to achieve desired resonances and bandwidths in a controlled manner. For easy understanding, this paper is categorized into six sections. Section 2 emphasizes on the working principle and the adopted design criteria for the creation of the produced design. Section 3 offers detailed insights into the employed ANN Ensembled approach and HSA operational procedure. A detailed discussion including optimized outcomes, software generated and experimentally produced outcomes associated with the Realized DSSFA is demonstrated in Section 4. To justify the novelty of the constructed design in Section 5, the performance of the Realized DSSFA is compared with some previously manufactured antennas. At the end, concluding remarks related to the presented research work are briefly revealed in Section 6.

Antenna design methodology

The improvised antenna is created iteratively by applying a staircase-shaped pattern on two opposite sides of the radiator along with a Sierpinski carpet (SC) fractal slot at the center of the upper-half portion. This meticulous design exhibits a symmetrical nature and multiband functionality. The detailed description of the step-by-step implementation of the Realized DSSFA is given in Fig. 1 (a–d). The key aspects associated with the design are particularly noteworthy.

The designed antenna is constructed physically on a Flame Retardant-4 (FR4) based dielectric slab of complete volume 26 × 32 × 1.6 mm^3. The specifications of the chosen, handy and financially manageable substrate are dielectric constant, $\varepsilon_r = 4.4$, flexural strength = 60,000 psi, and Poisson's ratio = 0.118 [16]. The geometrical construction begins with an initiator of size 20 × 26 mm^2, as illustrated in Fig. 1(a) (indicated as Stage I). In the 1st iteration, two equal sized rectangular blocks of dimensions (length = $\frac{1}{2}$th of the patch length and width = $\frac{1}{4}$th of the patch width) positioned at the top left and right corners, are etched from the parent geometry. Afterward, an SC fractal slot of dimensions "L_{S1}" ($\frac{1}{6}$th of the patch length) and "W_{S1}" ($\frac{1}{6}$th of the patch width) is embedded at the center of the upper-half portion of the geometry. The structure at this phase is named as Stage II (referred in Fig. 1b). The same design criterion is adopted for the development of Stage III (shown in Fig. 1c). Similarly, based on the above-said construction procedure, Stage IV (final shape, portrayed in Fig. 1d) is generated. The designed radiator is energized electromagnetically with a suitable 50 Ω microstrip feedline of dimensions "L_F" and "W_F". Here, the feedline is placed at a point away from the center (towards the right side of the y-axis). The predicted value of feed position and ground length achieved using the respective heterogeneous ANN Ensembled Model (described in Section 4.1) is utilized in the design process. For improved impedance matching, a slot loaded ground plane of dimensions "L_{GD}" and "W_{GD}" mm^2 is employed. Defected ground plane behaves as an impedance-matching element. It also offers modified current distribution and enhanced electromagnetic antenna characteristics. Further, it enables size reduction and multiband behavior. The resultant structure is named as modified Dual Staircase-Shaped Fractal Antenna (DSSFA). The complete structural arrangement of the Realized DSSFA (front and rear view) with labelled geometrical design parameters is illustrated in Fig. 2. The optimal design specifications of the Realized DSSFA are enlisted in Table 1.

Formulation of HSA-ANN Ensembled based integrated strategy

This section describes the generation procedure of a HSA-ANN Ensembled hybrid technique utilized in the designing process of the Realized DSSFA. In the first phase, two distinct heterogeneous ANN Ensembled Models are developed for the prediction of two critical design parameters belonging to the projected design. In the second phase, HSA approach is applied for the optimization of operating points. The well-trained Ensembled Models are employed in this phase for the formulation of the fitness function.

Projected ANN Ensembled model

For the development and analysis of a projected antenna design, standard empirical formulas/numerical equations are not available because of the complex structural design process [30]. Therefore, for such designs, soft computing approaches are very helpful as they offer acceptable answers within the specified range. One such approach is an ensembling of various ANNs bearing different

https://doi.org/10.1017/S1759078726103122 Published online by Cambridge University Press

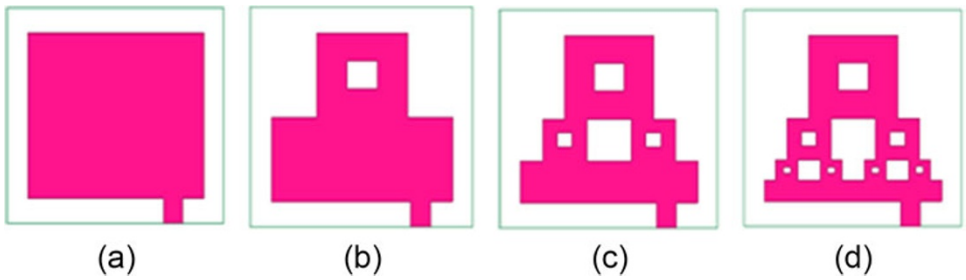


Figure 1. Development stages of Realized DSSFA (a) Stage I, (b) Stage II, (c) Stage III, and (d) Stage IV.
Stage I – 0th iteration; Stage II – 1st iteration; Stage III – 2nd iteration; Stage IV – 3rd iteration

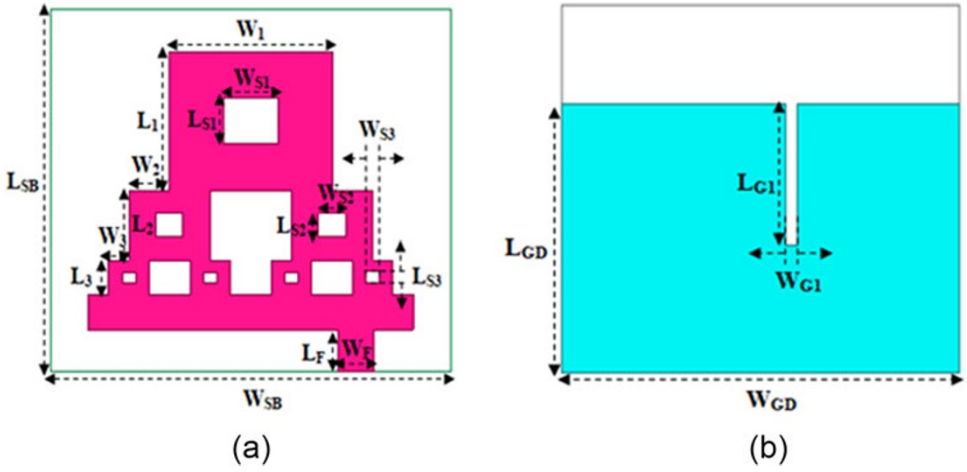


Figure 2. Realized DSSFA (a) final geometry, and (b) defected ground plane.

Table 1. Optimal design specifications of Realized DSSFA

L_{SB}	W_{SB}	L_1	W_1	L_2	W_2	L_3
26	32	10	13	5	6.5	2.5
W_3	L_{S1}	W_{S1}	L_{S2}	W_{S2}	L_{S3}	W_{S3}
3.25	3.33	4.33	1.67	2.16	0.833	1.083
L_F	W_F	L_{GD}	W_{GD}	L_{G1}	W_{G1}	
3.5	2.8	19	32	10	1	

All the parametric dimensions are in mm.

structural characteristics. In some situations, a single ANN model is not able to produce good generalization for data sets that exhibit complexity and show random errors [31]. Sometimes, a single ANN cannot handle large problems accurately. Therefore, there is a need to evaluate the outputs of different ANNs and then obtain the final output by averaging the previously computed outputs of each ANN model [32]. By doing so, the ensemble model shows good generalization performance in comparison to a single ANN.

In this work, two different heterogeneous ANN Ensembled Models have been developed for two distinct cases. For the given resonant frequencies ("f_{r1}," "f_{r2}," "f_{r3}," "f_{r4}," "f_{r5}," "f_{r6}," and "f_{r7}"), the first heterogeneous ANN Ensembled Model is developed to predict the feed position, whereas the second heterogeneous ANN Ensembled Model is implemented to predict the ground length [26]. In both cases, four different ANNs are chosen that include Feed Forward Back Propagation Network (FFBPN), Elman Neural Network (Elman NN), Generalized Regression Neural Network (GRNN), and Recurrent Neural Network (RNN). The outputs of these selected ANNs are aggregated and then the final ensembled output is taken by following the averaging method [33]. A detailed description of the ANN ensembling process is given in Fig. 3. The specifications of the chosen ANN models utilized in the ensembled process are given in Table 2.

The first heterogeneous ANN Ensembled Model has seven inputs: "f_{r1}" to "f_{r7}" and one output: the corresponding feed position. Likewise, the second heterogeneous ANN Ensembled Model has seven inputs ("f_{r1}" to "f_{r7}") and one output: the associated ground length. To generate the desired database, 90 DSSFAs are randomly created by choosing different feed positions. In the same manner, another set of 90 DSSFAs is generated randomly by taking different ground lengths. The above-said datasets are generated by varying feed positions between 18 and 26 mm (along y-axis) and ground lengths between 17 and 25 mm (along x-axis), respectively. In each case, 64 samples are defined for the training process

https://doi.org/10.1017/S1759078726103122 Published online by Cambridge University Press

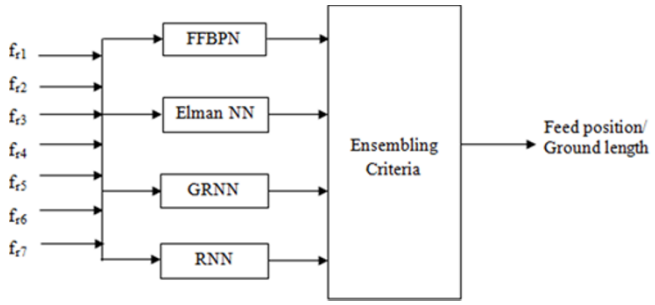


Figure 3. Heterogenous ANN Ensembled Model.

Table 2. Specifications of the chosen ANN models employed in ensembled process

S. No.	Network used	Number of hidden layers/ hidden layer neurons	Other details
1	FFBPN	2/10	Training function = Trainlm
			Data distribution = Random
			Adaptive learning function = Learngdm
			Transfer function = Tansig
2	Elman NN	2/12	Training function = Trainbfg
			Data distribution = Random
			Adaptive learning function = Learngdm
			Transfer function = Tansig
3	GRNN	2/20	Spread constant = 0.8
4	RNN	2/23	Spread constant = 0.6

and 26 samples are for the testing process. Here, for the proper selection of diverse training samples from the complete training database, the bootstrap aggregating method is employed. The function of this method is to create 4 different training subsets. The produced training subsets are utilized for the training of each ANN model. Thereafter, all the trained ANN models are tested using the provided test data and then ensembling is done.

Harmony search algorithm

Firstly introduced in the year 2001 by M. Kaur et al. [27], Harmony Search Algorithm (HSA) is a well-known and effective metaheuristic search approach that utilizes the pivotal principles associated with musicians' harmony improvisation. The instrument player repeatedly adjusts the pitch of the instrument by taking numerous combinations for the creation of the best possible outcome, termed as pleasing (best) harmony [28]. HSA employs a few adjustable parameters. HSA converges quickly to provide the best optimal solution corresponding to several difficult real-time optimization problems [29]. Harmony search illustrates solutions as harmonics by following the process of selection, pitch adjustment, and note creation (new) [34]. These predetermined harmonics are stored in Harmony Memory (HM).

The optimization problem of interest is given below [27]:

$$Min.\,(or\ Max) \qquad f\,(x_1, x_2, \ldots\ldots\ldots\ldots x_d) \tag{1}$$

Table 3. Format of HM

	x_1	x_2	–	x_d	f
Harmony 1	$x_{1,1}$	$x_{1,2}$	–	$x_{1,d}$	f_1
Harmony 2	$x_{2,1}$	$x_{2,2}$	–	$x_{2,d}$	f_2
	–	–	–	–	–
Harmony N	$x_{N,1}$	$x_{N,2}$	–	$x_{N,d}$	f_d

where f corresponds to the specified fitness function and x_i ($i = 1, 2, \ldots, d$) corresponds to the decision variable i.

The step-wise description of the employed HSA is given as:

Step 1 Initialization of control parameters. The related control parameters such as Harmony Memory Size (HMS), Harmony Memory Considering Rate (HMCR), Pitch Adjustment Rate (PAR), and the fret width (FW) are defined and assigned initially [28]. HMS specifies the maximum number of harmonics referred by the musician. HMCR refers to the probability at which the musician considers the randomly chosen harmony stored in HM [27]. PAR represents the probability of adjusting the chosen harmony. The value exhibited by the parameters (HMCR, PAR) lies between 0 to 1. FW depicts the pitch adjustment bandwidth. HMCR is used to adjust the exploration, whereas PAR and FW are employed to adjust the exploitation [29].

Step 2 Initialization of Harmony Memory. In the possible solution (search) space, N harmonics are stochastically created and placed suitably in HM [34]. Harmony corresponds to the set of notes decided by the musician. In particular, Harmony i can be represented as $[x_{i,1}x_{i,2} \ldots\ldots\ldots x_{i,d}]$. For HM initialization, the employed empirical formula is given below [27]:

$$x_{i,j} = l_j + rand\,(u_i - l_j)\; i = 1, 2, \ldots\ldots\ldots N$$
$$j = 1, 2, \ldots\ldots\ldots d \tag{2}$$

where l_j depicts the lower bound related to the decision variable j and u_j reveals the upper bound related to the same decision variable [28]. rand represents the randomly produced value in the span interval [0,1]. Table 3 delineates the representation of HM in which the column at the last reveals the fitness function value corresponding to each harmony [27].

Step 3 Improvisation. In this step, a new harmony is improvised by following the process of recombination and mutation [29]. The newly created harmony is expressed as $x_{new} = [x_{new,1}x_{new,2} \ldots\ldots\ldots x_{new,d}]$. Using HMCR, each component associated with the new harmony is examined. With a probability PAR, pitch adjustment is applied if the examined component belongs to the set of existing harmonics [27]. FW depicts the step size of the associated movement. All such actions result in the creation of new harmony [34].

Step 4 Updating the Harmony Memory. The fitness value belonging to the new harmony is evaluated. Afterward, the examined fitness value and the fitness value related to the worst harmony are compared [27]. If the evaluated fitness corresponding to the new harmony is better than the worst member's fitness then the new harmony replaces the worst harmony [29]. Contrarily, there is no need for such a replacement.

https://doi.org/10.1017/S1759078726103122 Published online by Cambridge University Press

https://doi.org/10.1017/S1759078726103122 Published online by Cambridge University Press

Table 4. Estimation of feed position for test data using different ANN models/First heterogenous ANN Ensembled Model

	Resonant frequencies (GHz) (inputs)							Feed position (mm) (output) obtained using						
S. No.	f_{r1}	f_{r2}	f_{r3}	f_{r4}	f_{r5}	f_{r6}	f_{r7}	FFBPN	Elman NN	GRNN	RNN	ANN ensemble	Desired value	Computed error
1	2.4309	3.5812	4.2265	7.6648	8.8015	11.9699	14.3828	21.2439	21.0399	21.1494	21.0029	21.1090	21	−0.1090
2	2.4589	3.5812	4.2265	7.6512	8.8196	11.8831	14.3267	19.3032	21.0261	21.1505	21.0023	20.6205	21.3	0.6794
3	2.4309	3.5812	4.2265	7.6629	8.7996	11.7725	14.5234	21.6014	21.5765	21.6000	21.0001	21.4445	21.6	0.1554
4	2.4589	3.5812	4.2545	7.6493	8.7715	11.9138	14.2705	21.7040	21.9619	22.3241	21.7964	21.9466	21.7	−0.2466
5	2.4028	3.5812	4.2265	7.6493	8.7715	11.9419	14.4108	21.8120	22.3092	23.3344	21.2562	22.1779	21.8	−0.3779
6	2.4589	3.6092	4.2589	7.6212	8.7154	11.8858	14.3828	22.1282	22.1345	22.3260	21.9919	22.1451	21.9	−0.2451
7	2.4309	3.5812	4.2265	7.6774	8.7154	11.8297	14.4108	21.6146	22.3151	22.3153	22.1927	22.1094	22.3	0.1905
8	2.4589	3.5812	4.2265	7.6774	8.7154	11.8858	14.4108	22.1131	22.2703	20.3254	22.1947	21.7259	22.35	0.6240
9	2.4589	3.6092	4.2265	7.7054	8.7435	11.9138	14.4108	22.2527	22.1646	22.3300	22.0040	22.1878	22.4	0.2121
10	2.4875	3.6092	4.2265	7.6774	8.6874	12.8116	14.3547	22.5378	22.5052	22.5345	22.3538	22.4828	22.5	0.0171
11	2.4589	3.5812	4.2265	7.7054	8.7435	11.8297	14.5511	22.6099	22.5544	22.3217	22.5846	22.5176	22.6	0.0823
12	2.4873	3.5812	4.2545	7.7054	8.6874	12.9238	14.6072	22.6644	22.7027	22.5784	22.8033	22.6872	22.65	−0.0372
13	2.4877	3.6092	4.2545	7.7335	8.7154	12.9238	14.5235	23.3604	22.6691	22.5725	24.2885	23.2226	22.7	−0.5226
14	2.4028	3.6092	4.2265	7.7615	8.7435	12.9801	14.6353	22.8068	22.7765	22.5869	22.6081	22.6946	22.8	0.1053
15	2.4589	3.5812	4.1984	7.6212	8.6593	12.9843	14.6072	23.1012	23.0376	22.5879	22.9755	22.9255	23.1	0.1744
16	2.4879	3.6092	6.1092	7.6774	8.6593	13.0086	14.6633	23.4012	23.3173	23.3766	23.0490	23.2861	23.3	0.0138
17	2.4589	3.6092	6.0501	7.7054	8.6593	12.9519	14.6072	23.3873	23.3173	25.3533	23.1524	23.8026	23.35	−0.4526
18	2.4589	3.6092	6.1092	7.6774	8.6593	12.9519	14.6353	23.3193	23.3501	23.3708	23.1114	23.2879	23.4	0.1120
19	2.4873	3.6092	6.0782	7.7054	8.6593	13.0087	14.6353	23.3887	23.3023	23.3678	23.0759	23.2837	23.5	0.2162
20	2.4589	3.6092	6.1062	7.7054	8.6412	13.0361	14.6072	23.7035	23.7750	23.8249	23.8441	23.7869	23.7	−0.0869
21	2.4589	3.6092	4.2265	6.1062	7.6774	13.0081	14.4108	23.8024	22.9300	23.2998	23.6221	23.4136	23.8	0.3863
22	2.4874	3.5812	6.1062	7.6774	8.6313	13.0083	14.5792	23.8809	25.7701	23.5448	23.6766	24.2181	23.9	−0.3181
23	2.4876	3.6092	6.1062	7.6774	7.9925	13.0361	14.6072	24.0920	23.9340	23.8250	23.9423	23.9483	23.95	0.0016
24	2.4878	3.6092	6.1542	6.1623	7.9812	13.1202	14.5232	24.2075	24.1519	24.6285	24.1365	24.2811	24.15	−0.1311
25	2.4877	3.6092	6.2214	6.1623	8.0526	13.1764	14.7756	24.1520	24.1770	24.2160	26.1336	24.6696	24.2	−0.4696
26	2.4872	3.6092	6.1854	6.1062	8.5412	13.0361	14.5238	24.2108	24.1434	24.2171	24.1073	24.1697	24.3	0.1303
Mean Computed Error $\|e\|$														0.0040

https://doi.org/10.1017/S1759078726103122 Published online by Cambridge University Press

Table 5. Estimation of ground length for test data using different ANN models/Second heterogenous ANN Ensembled Model

	Resonant frequencies (GHz) [Inputs]							Ground length (mm) [Output] obtained using						
S. No.	f_{r1}	f_{r2}	f_{r3}	f_{r4}	f_{r5}	f_{r6}	f_{r7}	FFBPN	Elman NN	GRNN	RNN	ANN ensemble	Desired value	Computed error
1	2.5711	3.8898	4.7595	5.9659	8.7715	11.8577	15.0125	17.9972	18.2870	18.9395	18.4006	18.4061	17	−1.4061
2	2.5711	3.8617	4.7315	5.9854	8.7996	11.8452	14.8878	18.2804	18.1618	18.9262	18.0038	18.3431	17.2	−1.1431
3	2.5431	3.8337	4.7034	5.9941	8.7435	11.8577	14.8878	18.1437	19.3902	18.4770	17.1423	18.2883	17.3	−0.9883
4	2.5431	3.7776	4.5351	8.1543	8.6593	11.8577	14.5792	18.6303	17.1593	18.3662	18.7919	18.2369	17.7	−0.5369
5	2.4876	3.6934	4.3948	8.0143	8.5471	11.8297	14.2986	19.2218	18.6261	19.3691	18.9993	19.0541	18	−1.0541
6	2.4711	3.6934	4.4793	7.9916	8.3226	11.8016	14.6914	19.8253	19.1503	18.1000	18.0755	18.7877	18.1	−0.6877
7	2.4431	3.7214	4.4798	7.9865	8.7154	11.9419	14.6353	18.9472	19.1488	19.6841	19.1104	19.2226	18.2	−1.0226
8	2.4515	3.6653	4.3387	7.8737	8.5752	11.7455	14.3547	20.0862	19.5515	19.3526	18.3403	19.3326	18.3	−1.0326
9	2.4311	3.6653	4.2028	7.8457	8.7154	11.8577	14.7475	19.1177	19.1309	18.3599	19.5200	19.0321	18.4	−0.6321
10	2.4287	3.6373	4.2826	7.7335	8.6874	12.9843	14.5239	18.9164	18.4535	19.6377	18.8508	18.9646	18.7	−0.2646
11	2.4288	3.6373	4.2826	7.7615	8.6874	13.0086	14.5235	18.9156	18.4627	18.6429	18.9555	18.7442	18.8	0.0557
12	2.4309	3.6092	4.1984	7.7054	8.6874	12.9238	14.4108	21.4172	19.6377	18.6271	19.8937	19.8939	19	−0.8939
13	2.4628	3.6251	5.2926	7.4813	8.7435	12.6433	13.9058	19.2322	20.3983	19.0270	19.0403	19.4244	19.1	−0.3244
14	2.4315	3.6189	5.2645	7.7054	8.6874	12.5872	14.0187	18.3898	19.2842	20.9252	21.4006	19.9999	19.2	−0.7999
15	2.4486	3.3206	6.0782	7.6493	8.6593	12.5311	13.9913	20.7848	19.7312	21.2823	20.4025	20.5502	19.3	−1.2502
16	2.7596	3.2365	6.1062	7.4693	8.6874	12.5872	13.9900	18.5211	19.8021	20.3060	19.5503	19.5449	19.4	−0.1449
17	2.9928	3.2365	6.1343	7.6212	8.6874	12.5591	14.0187	20.1798	19.8372	20.2844	20.6057	20.2268	19.6	−0.6268
18	3.0481	3.2365	6.0782	7.5651	8.6593	12.3627	13.9339	20.0952	19.9543	20.3356	19.8785	20.0659	20.1	0.03406
19	3.0481	3.2084	6.0782	7.5098	8.6032	12.2505	13.7936	20.7574	20.5239	20.3966	20.4973	20.5438	20.4	−0.1438
20	3.0481	3.1804	6.0782	7.5097	8.6313	12.2786	13.7655	19.5252	21.5414	21.3930	21.1158	20.8939	20.6	−0.2939
21	3.0481	3.1804	6.0782	7.4816	8.6593	12.3066	13.7094	20.5606	21.5640	21.9011	21.4836	21.3773	20.7	−0.6773
22	3.0481	3.0962	6.7234	7.0882	8.4068	12.1383	13.1764	21.3828	21.4527	20.7642	21.8903	21.3725	20.9	−0.4725
23	2.9639	3.0962	6.5551	7.1723	8.4349	11.9983	13.9058	21.7635	21.2141	21.8167	22.4519	21.8115	21.45	−0.3615
24	2.9924	3.0962	6.4429	7.0882	8.4349	12.1102	13.7936	22.1737	21.2156	20.6077	21.4209	21.3545	21.6	0.24547
25	3.0243	3.1804	6.0782	6.6393	7.3687	9.8657	12.1383	22.5686	23.9033	22.8944	21.8168	22.7958	21.92	−0.8758
26	3.1144	3.1242	6.3868	7.0321	8.4349	12.0822	13.3166	23.9099	23.6801	20.8988	23.8190	23.0770	23.15	0.07299
Mean Computed Error $\|e\|$														0.5856

Table 6. Performance measures obtained from different ANN models/First heterogenous ANN Ensembled Model in regard to feed position estimation

Network type	MCE	MAE	MSE	RMSE	*R*-squared(%)
FFBPN	0.0057	0.0002	0.0962	0.3101	96
Elman NN	0.0398	0.0016	0.1011	0.3180	93
GRNN	0.0295	0.0010	0.1547	0.3933	94
RNN	0.1670	0.0073	0.1298	0.3603	92
ANN ensemble	**0.0040**	**0.0002**	**0.0897**	**0.2995**	**98**

Table 7. Performance measures obtained from different ANN models/Second heterogenous ANN Ensembled Model in regard to ground length estimation

Network type	MCE	MAE	MSE	RMSE	*R*-squared (%)
FFBPN	0.5875	0.0315	0.9740	0.9869	95
Elman NN	0.5924	1.0309	0.8004	0.8946	93
GRNN	0.5984	1.0325	1.2416	1.1143	92
RNN	0.5899	1.0310	0.7025	0.8381	94
ANN Ensemble	**0.5856**	**0.0314**	**0.5382**	**0.7336**	**96**

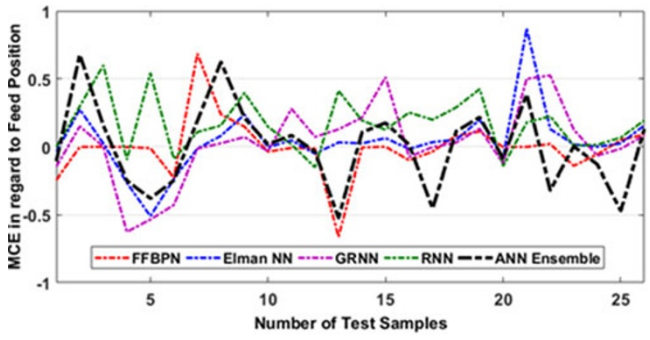


Figure 4. MCE against number of test samples in regard to feed position estimation.

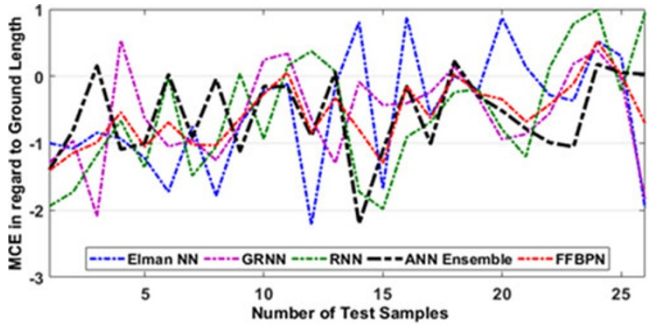


Figure 5. MCE against number of test samples in regard to ground length estimation.

Step 5 Termination Criterion. The above-described two steps (steps 2 and 3) are repeated until the pre-defined termination criterion is met [27]. When this condition is fulfilled, the algorithm stops and the final outcome is noted.

Step 6 Final result. This step gives the optimal solution to the concerned optimization problem. The provided optimal answer corresponds to the best harmony.

For the implementation of Realized DSSFA, an HSA-ANN Ensembled integrated approach is developed to achieve the desired frequency bands (2.43, 3.61, 4.20, 7.71, 8.69, 12.90, and 14.41 GHz). Based on the pre-defined goals, the formulated fitness function associated with the HSA is described in Eq. (3) [27]. In the derived equation, trained heterogeneous ANN Ensembled Models are employed to provide the values of feed position and ground length. During the optimization process, the fitness function converges to a minimum value so that the Realized DSSFA can resonate at the defined operating bands.

$$\text{Fitness function } = \alpha(F_{Pi} - F_{PANN})^{1/2} + \beta(L_{GDi} - L_{GDANN})^{1/2} \tag{3}$$

where α and β correspond to the control variables

Results and discussion

To demonstrate the reliability and supremacy of the Realized DSSFA, numerical simulations, computational analysis and experimental investigations are thoroughly exemplified in this section.

Computational analysis using developed ANN ensembled models

In this subsection, the performance of the developed ANN Ensembled Models has been analyzed and compared with the selected ANN models. The two distinct heterogeneous ANN Ensembled Models have been applied for exact prediction of two preliminary design parameters associated with the Realized DSSFA, i.e., feed position and ground length. After a deep parametric analysis, training and test datasets are generated. The quality of these models is recorded by evaluating the value of Mean Computed Error (MCE), Mean Absolute Error (MAE), Mean Square Error (MSE), Root Mean Square Error (RMSE), and *R*-squared [30]. All the above-said performance metrics are numerically computed by Eqs. (4–8) [32, 35].

$$MCE = \left| \frac{1}{n} \sum_{k=1}^{n} \left(O_k - \widehat{O}_k \right) \right| \tag{4}$$

https://doi.org/10.1017/S1759078726103122 Published online by Cambridge University Press

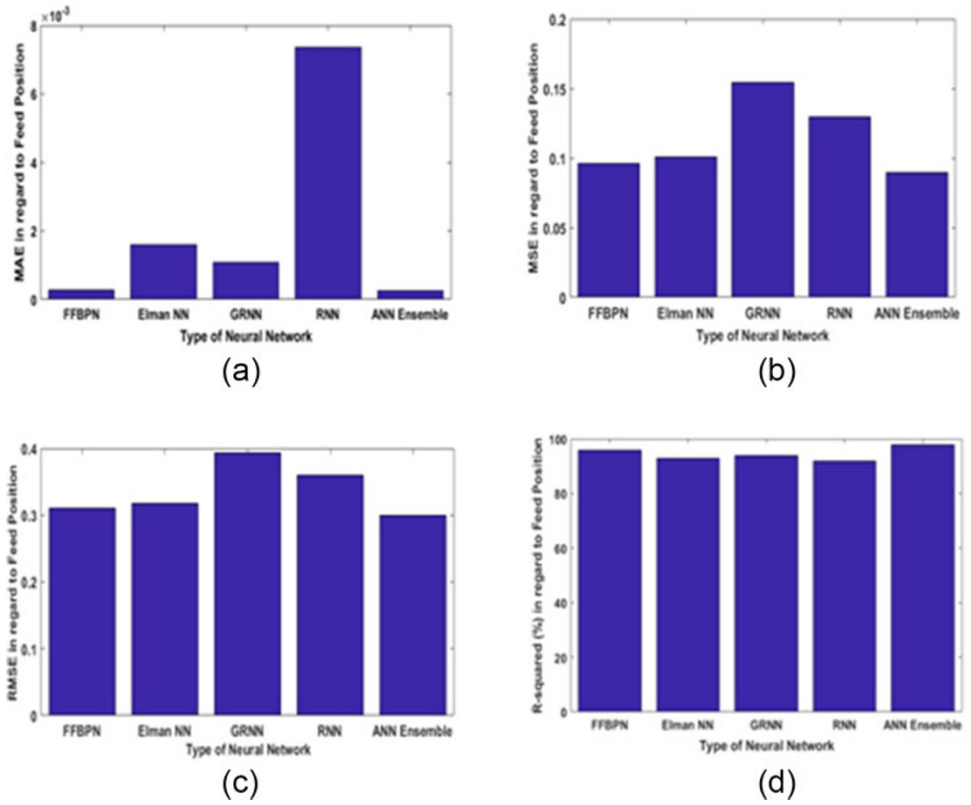


Figure 6. Performance assessment measures obtained from selected ANN models/First heterogenous ANN Ensembled Model in regard to feed position estimation (a) MAE, (b) MSE, (c) RMSE, and (d) *R*-squared (%).

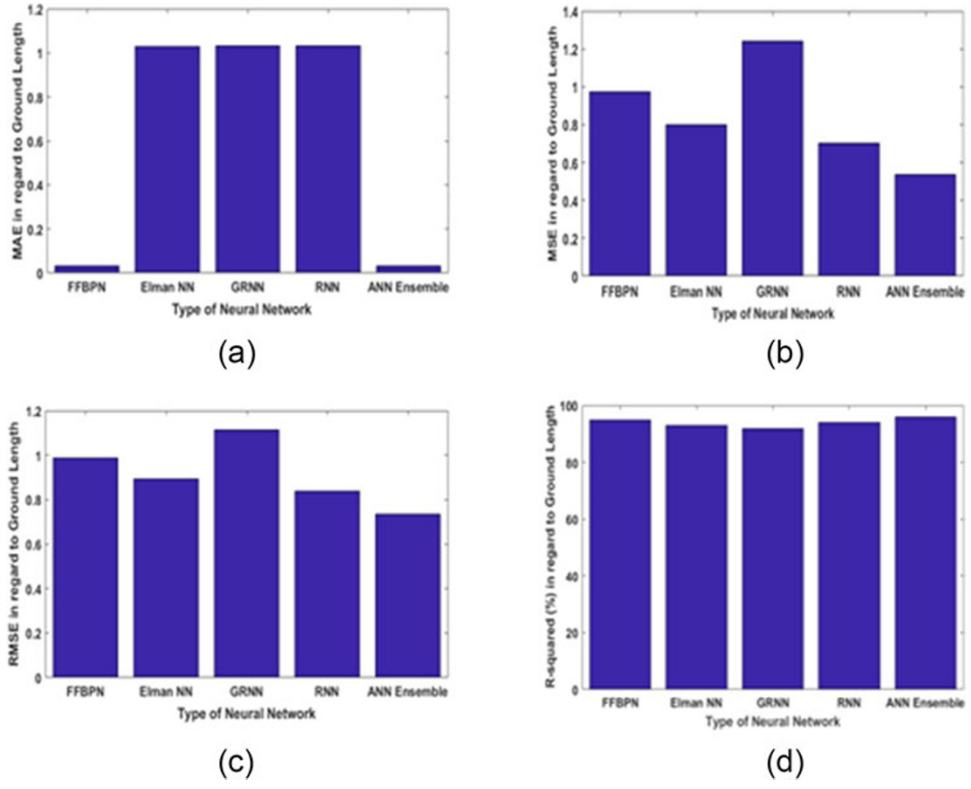


Figure 7. Performance assessment measures obtained from different ANN models/Second heterogenous ANN Ensembled Model ANN Ensemble in regard to ground length estimation (a) MAE, (b) MSE, (c) RMSE, and (d) R-squared(%).

https://doi.org/10.1017/S1759078726103122 Published online by Cambridge University Press

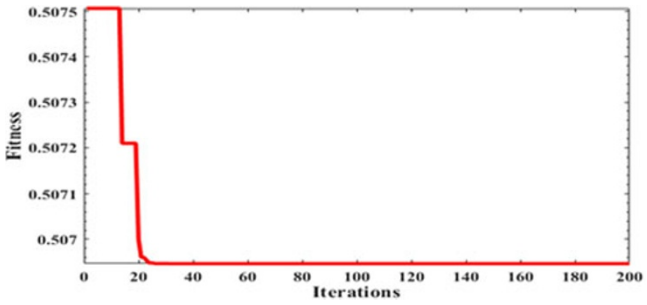


Figure 8. Fitness value associated with the HSA-ANN Ensembled based integrated approach.

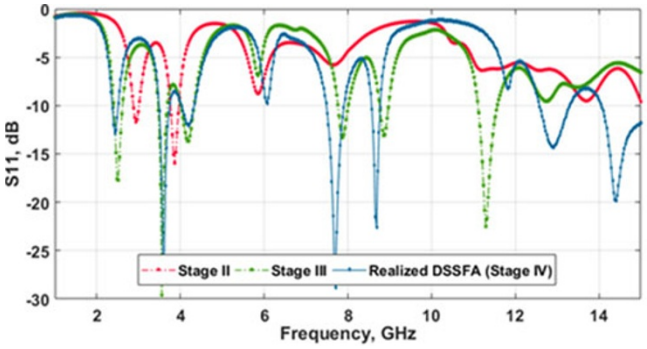


Figure 9. S11 characteristics of the Realized DSSFA at three different development stages.

$$MAE = \frac{1}{n}\sum_{k=1}^{n}\left|O_k - \widehat{O}_k\right| \tag{5}$$

$$MSE = \frac{1}{n}\sum_{k=1}^{n}\left(O_k - \widehat{O}_k\right)^2 \tag{6}$$

$$RMSE = \sqrt{\frac{1}{n}\sum_{k=1}^{n}\left(O_k - \widehat{O}_k\right)^2} \tag{7}$$

$$R^2 = 1 - \frac{\sum_{k=1}^{n}\left(O_k - \widehat{O}_k\right)^2}{\sum_{k=1}^{n}\left(O_k - \bar{O}\right)^2} \tag{8}$$

where O_k specifies the actual output, $\widehat{O}_k$ reveals the predicted output, $\bar{O}$ represents the mean output value, and n indicates the number of samples.

All the obtained results regarding the estimation of feed position for test data using different ANN models/First heterogenous ANN Ensembled Model are summarized in Table 4. The estimated value of feed position computed using different ANN models (FFBPN, Elman NN, GRNN, RNN), and the developed heterogenous ANN Ensembled Model (first one) is compared with the desired value. From Table 4, it is found that the examined value of MCE is 0.0040. Similarly, Table 5 illustrates all the resultant outcomes regarding the estimation of ground length for test data using different ANN models/Second heterogenous ANN Ensembled Model. Here, the value of ground length estimated using FFBPN, Elman NN, GRNN, RNN, and the developed heterogenous ANN Ensembled Model (second one) is compared with the desired value. Thereafter, the value of MCE is calculated and found as 0.5856. Generally, small value of MCE delineates high predictive accuracy, whereas large value indicates low predictive accuracy. Desired performance measures evaluated from distinct ANN models/First heterogenous ANN Ensembled Model in regard to the feed position estimation are described in Table 6. On the other hand, Table 7 summarizes the values of desired performance indicators evaluated from distinct ANN models/Second heterogenous ANN Ensembled Model in regard to the ground length estimation. Among all these presented ANN models, it is demonstrated that the resultant First/Second heterogenous ANN Ensembled Models reveal high prediction accuracy in comparison to other selected ANNs.

The graphical representation of MCE obtained using the selected ANN models/First heterogenous ANN Ensembled Model against number of test samples in regard to feed position estimation is given in Fig. 4. The values of MCE obtained using selected ANN models/Second heterogenous ANN Ensembled Model against number of test samples in regard to ground length estimation are graphically delineated in Fig. 5. Performance assessment measures (MAE, MSE, RMSE, and R-squared(%)) obtained from all selected ANN models/First heterogenous ANN Ensembled Model in regard to feed position estimation are displayed in Fig. 6(a–d). Similarly, the critical performance assessment measures (MAE, MSE, RMSE, and R-squared [%]) obtained from the selected ANN models/Second heterogenous ANN Ensembled Model in regard to ground length estimation are displayed statistically in Fig. 7(a–d).

HSA-ANN Ensembled based integrated approach results

In HSA, number of harmonics "N" is assumed as 18 and the maximum number of iterations is taken as 200. The initially specified values of "HMS," "HMCR," "PAR," and "FW" are 36, 0.95, 0.7, and 0.07, respectively. Effective hyperparameter tuning largely depends on the control on these parameters in order to balance global exploration and local exploitation. Hence, it helps in achieving improved convergence reliability. Optimization results characterize that the recommended hybrid algorithm converges to an value of 0.5069 after 24 iterations, as depicted in Fig. 8. The examined optimized values of "f_{r1}," "f_{r2}," "f_{r3}," "f_{r4}," "f_{r5}," "f_{r6}," and "f_{r7}" are 2.4256, 3.6081, 4.2115, 7.7216, 8.6884, 12.8992, and 14.4009 GHz, respectively.

Realized DSSFA results

The design, characterization and implementation of the aforementioned antenna structure are carried out using an efficient simulation tool, v.15 Ansoft High-Frequency Structure Simulator (HFSS) [7]. The innovative and uncomplicated fractal geometry exhibits two salient features: concision and multiband operation [36]. For analysis purposes, the spanning range chosen is 1 to 15 GHz. Figure 9 explicates the S11 characteristics of the Realized DSSFA at three different development stages. Results demonstrate that Stage II (1st iteration) produces two resonant bands, centered at 2.94 and 3.86 GHz with −10 dB impedance bandwidth (IBW) of 5.4% (2.86–3.02 GHz) and 5.7% (3.75-3.97 GHz), respectively. Subsequently, at Stage III (2nd iteration), six operational bands are examined. The recognized resonant points are 2.52, 3.55, 4.17, 7.87, 8.86, and 11.30 GHz. The noted Voltage Standing Wave Ratio (VSWR) values are ≤2, claiming good impedance matching. The final design (Stage IV/3rd iteration/Realized DSSFA) resonates at seven points within the above-specified frequency range.

https://doi.org/10.1017/S1759078726103122 Published online by Cambridge University Press

Table 8. Performance comparison between three different development stages

Stage no.	"F_L" (GHz)	"F_R" (GHz)	"F_H" (GHz)	S11 (dB)	BWR	VSWR
Stage II (1st iteration)	2.86	2.94	3.02	−11.69	1.06	1.74
	3.75	3.86	3.97	−15.95	1.06	1.38
Stage III (2nd iteration)	2.40	2.52	2.62	−17.72	1.09	1.29
	3.46	3.55	3.64	−13.68	1.05	1.52
	4.00	4.17	4.33	−13.33	1.08	1.54
	7.76	7.87	8.01	−13.10	1.03	1.61
	8.75	8.86	8.97	−22.50	1.02	1.17
	11.11	11.30	11.58	−29.60	1.04	1.06
Realized DSSFA (Stage IV) (3rd iteration)	2.35	2.43	2.52	−12.86	1.07	1.58
	3.47	3.61	3.75	−27.43	1.08	1.08
	4.03	4.20	4.35	−12.05	1.08	1.67
	7.48	7.71	7.90	−28.84	1.05	1.07
	8.57	8.69	8.77	−22.57	1.02	1.16
	12.56	12.90	13.32	−14.28	1.06	1.48
	14.07	14.41	> 15.00	−19.82	> 1.07	1.23

First band [Band-1] spans from 2.35 to 2.52 GHz, centered at 2.43 GHz and offers −10 dB IBW of 6.9%. Second band [Band-2] is centered at 3.61 GHz with a spanning range of 3.47–3.75 GHz (−10 dB IBW = 7.7%). Likewise, the Third band [Band-3] resonates at 4.20 GHz and the S11 is −12.05 dB. Fourth band [Band-4] lies in the range of 7.48-7.90 GHz. Here, the resonance is observed at 7.71 GHz. The linked S11 and VSWR are −28.84 dB and 1.07, respectively. Fifth band [Band-5] has a dominant frequency = 8.69 GHz and −10 dB IBW = 2.3%. The resonance and S11 associated with the sixth band [Band-6] is 12.90 GHz and −14.28 dB, respectively. The prominent resonance related to the seventh band [Band-7] is 14.41 GHz. The corresponding S11 is −19.82 dB and the −10 dB IBW is greater than 6.4%. Importantly, as a proof of concept, resonance lowering and enhancement in operational bands have been examined from Fig. 9. Additionally, the demonstrated fractal configuration offers a 33% size reduction. For a more reasonable explanation, performance comparison between three different development stages is illustrated in Table 8. Moreover, the S11 characteristics of the Realized DSSFA with/without incorporation of SC fractal are compared in Fig. 10. From this plot, it can be inferred that Realized DSSFA without incorporation of SC fractal offers six resonant bands, whereas the SC fractal incorporated projected design produces seven resonant bands. For more understanding, S11 characteristics of the Realized DSSFA with Defected Ground/Full Ground are compared in Fig. 11.

Based on the dimensional geometry, as portrayed in Fig. 2, the antenna is fabricated. The hardware model of the Realized DSSFA joined with a suitable 50 Ω connector is portrayed in Fig. 12. The precisely constructed antenna structure is employed for experimentation. S11 characteristics are extracted using an Analyzer present in the microwave laboratory. For clear perception, the computed S11 values (software generated/experimentally extracted) are illustrated in Fig. 13. Practically computed measurements depict that the hardware model produces resonance at 2.48, 3.58, 4.25, 7.65, 8.74, 11.83, and 14.44 GHz with an associated Bandwidth Ratio (BWR) of 1.07, 1.07, 1.07, 1.04, 1.02, 1.02, and 1.06. After careful examination of the plot, a good

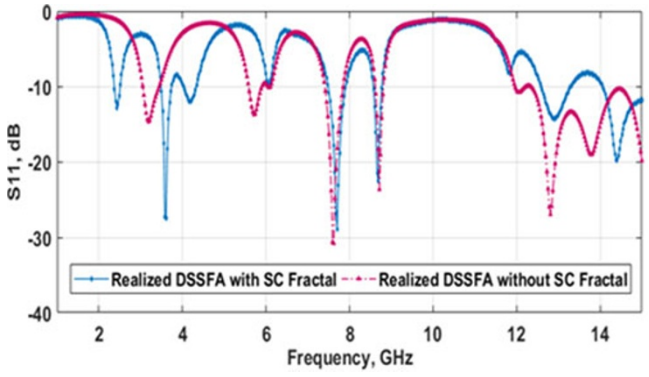


Figure 10. S11 characteristics of the Realized DSSFA with/without incorporation of SC fractal.

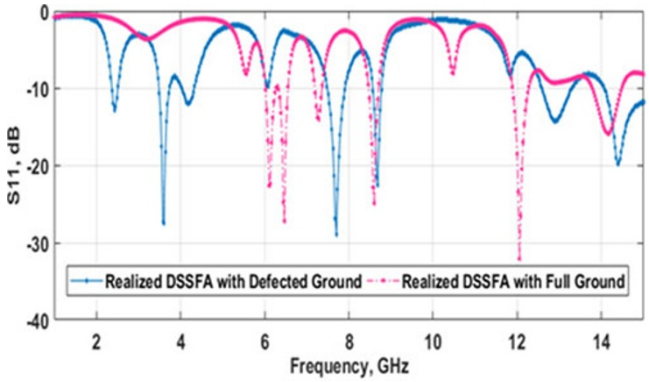


Figure 11. S11 characteristics of the Realized DSSFA with Defected Ground/Full Ground.

resemblance between the software generated and experimentally extracted values is noted. Minor deviations are due to the measured apparatus errors, human errors, substrate inconsistency, disturbed environmental conditions, and insertion losses of connector and

https://doi.org/10.1017/S1759078726103122 Published online by Cambridge University Press

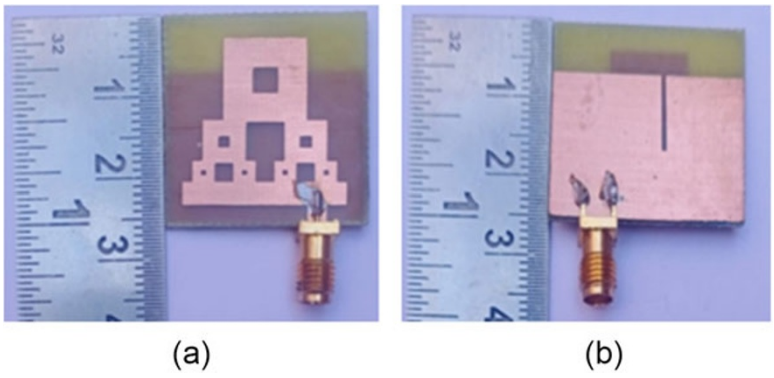


Figure 12. FR4 based developed DSSFA (a) Front side, and (b) Back side.

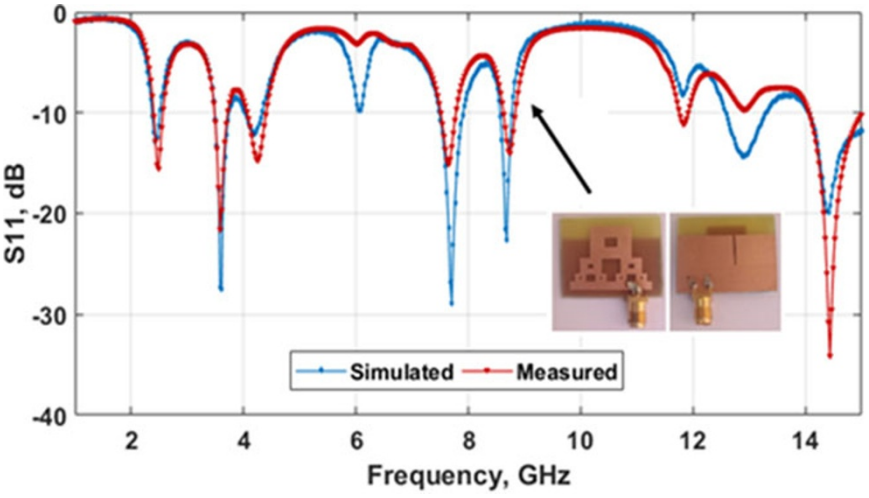


Figure 13. Simulated and experimentally extracted S11 behavior of the Realized DSSFA.

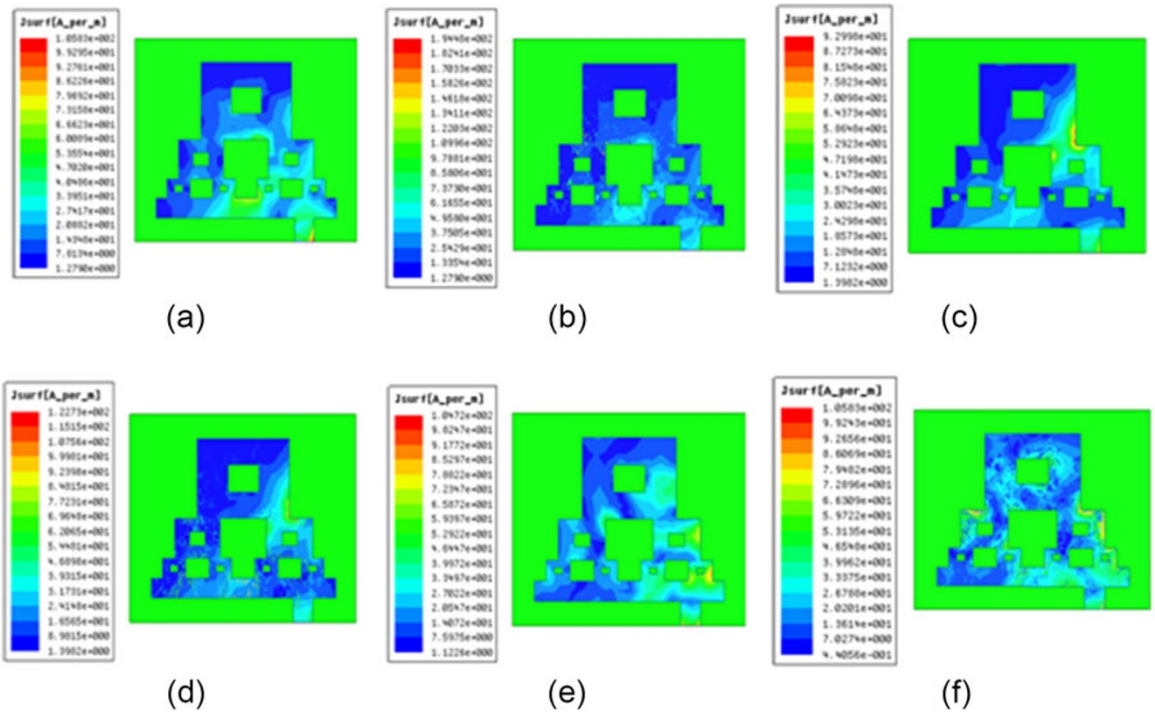


Figure 14. Current distribution on Realized DSSFA's surface at (a) 2.43, (b) 4.20, (c) 7.71, (d) 8.69, (e) 12.90, and (f) 14.41 GHz operational frequency points.

https://doi.org/10.1017/S1759078726103122 Published online by Cambridge University Press

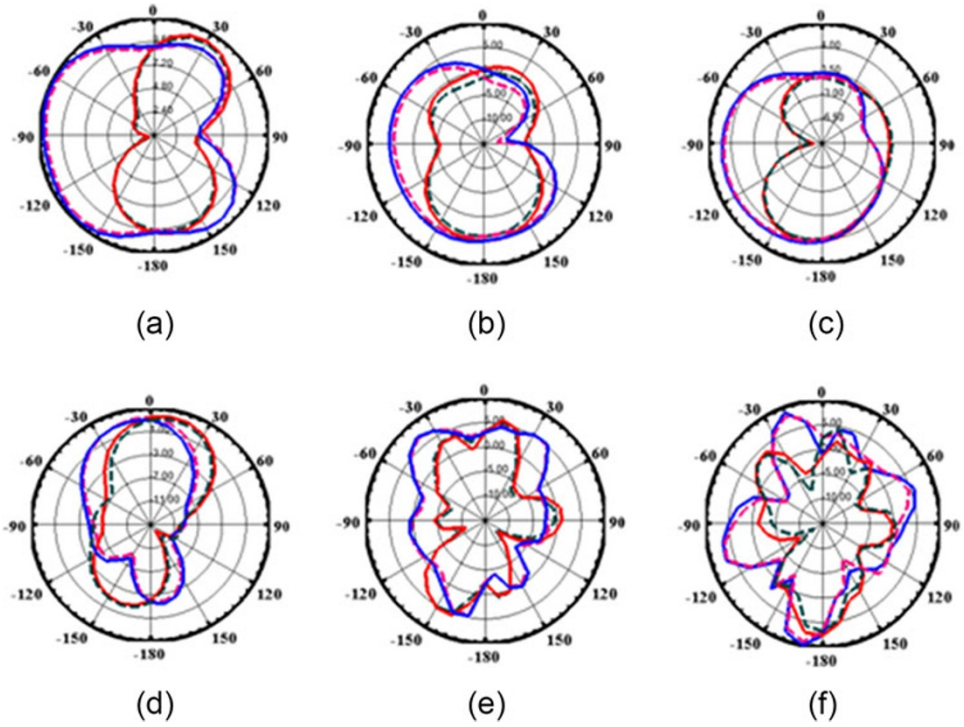


Figure 15. Simulated/software generated (solid line in blue and red color) and measured/experimentally extracted (dashed line in pink and green color) radiation patterns in regard to *E* and *H* planes of Realized DSSFA (a) 2.43, (b) 4.20, (c) 7.71, (d) 8.69, (e) 12.90, and (f) 14.41 GHz operational frequency points.

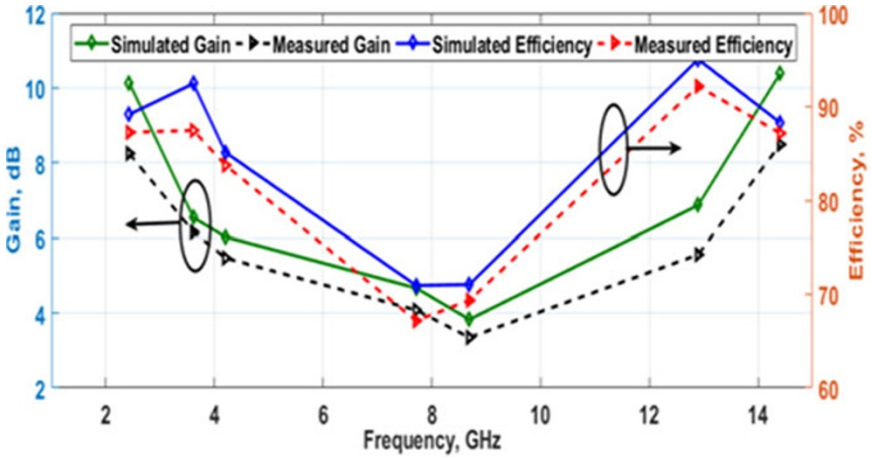


Figure 16. Simulated and practically revealed gain and efficiency values of the Realized DSSFA.

cable [37]. Hence, the experimental observations clearly reveal that the suggested design is an excellent competitor for Wireless Local Area Network (WLAN) (IEEE 802.11 b/g/n), Energy harvesting, Industrial, Scientific and Medical (ISM) band, Radio Frequency Identification (RFID), Amateur radio, Maritime mobile, Fixed mobile except aeronautical mobile, Direct broadcast satellite, Radio astronomy, Radio navigation, and Space research.

The working mechanism of the Realized DSSFA can be clearly examined by plotting the current distribution plots at six investigated resonances, namely, 2.43, 4.20, 7.71, 8.69, 12.90, and 14.41 GHz, as demonstrated in Fig. 14. In this investigation, it is possible to comprehend the regions that contribute to multiband frequencies [34]. At 2.43 GHz, the current flow is prominent at the lower right portion of the designed patch. On the other side, the lower left and upper portions have weak currents. At 4.20 GHz, maximum circulation of current is around/near the center portion of the patch and the feed. Corresponding to 7.71/8.69 GHz, current is more concentrated at the lower, upper right portion of the radiator and the feed. At higher resonances (12.90/14.41 GHz), current is homogenously dispersed at the Realized DSSFA's surface. From Fig. 14(a–f), it can be inferred that the etched fractal slots perturb the current path resulting in the appearance of additional resonances at higher values without increasing the antenna size. For the far-field analysis, reliable and consistent experimentation is done in an anechoic chamber. A standard pyramidal horn antenna bearing characteristics such as gain, "G_T" = 8.5 dB and transmitting power, "P_T" = 1 mW works as a reference antenna. The manufactured prototype is placed at the opposite end of the standard antenna device. The outcomes are recorded step-wise by varying the rotation angle from 0° to 360°. To eliminate the reflections, anechoic

https://doi.org/10.1017/S1759078726103122 Published online by Cambridge University Press

Table 9. Software generated and experimentally extracted performance behavior of Realized DSSFA

Results	"F_L" (GHz)	"F_R" (GHz)	"F_H" (GHz)	S11 (dB)	BWR	VSWR
Simulated	2.35	2.43	2.52	−12.86	1.07	1.58
	3.47	3.61	3.75	−27.43	1.08	1.08
	4.03	4.20	4.35	−12.05	1.08	1.67
	7.48	7.71	7.90	−28.84	1.05	1.07
	8.57	8.69	8.77	−22.57	1.02	1.16
	12.56	12.90	13.32	−14.28	1.06	1.48
	14.07	14.41	>15.00	−19.82	>1.07	1.23
Measured	2.40	2.48	2.57	−15.54	1.07	1.40
	3.47	3.58	3.72	−21.60	1.06	1.18
	4.10	4.25	4.40	−14.72	1.07	1.45
	7.50	7.65	7.78	−15.11	1.04	1.53
	8.63	8.74	8.85	−13.99	1.02	1.49
	11.73	11.83	11.93	−11.12	1.02	1.76
	14.07	14.44	14.99	−34.11	1.06	1.04

Table 10. Comparison of Realized DSSFA with certain prior reported antennas

Ref. no.	Electricalsize (λ_0^2)	Resonances (GHz)	Bandwidth (MHz)	Gain (dB)	Remarks
[2]	$0.32\lambda_0 \times 0.35\lambda_0$	2.45/3.85/7.10/ 9.40	200/6120	1.47 (max)	Ultraband features but large size and poor gain
[3]	$0.44\lambda_0 \times 0.49\lambda_0$	2.53/4.91/7.6	178/4.75/334	8.61/3.32/5.38	Decent gain but large volume
[7]	$0.27\lambda_0 \times 0.27\lambda_0$	2.42/5.80	35/25	10.19/5.74	High gain but moderate size
[10]	$0.4\lambda_0 \times 0.4\lambda_0$	2.4/6/8.2	410/1070/4840	3.27/4.37/5.52	Adorable gain and bandwidth but very large volume
[12]	$0.32\lambda_0 \times 0.24\lambda_0$	1.98/5.94/10.61/ 12.73/14.85	2830/1700/280/ 710/570	8.4/1.2/1.9/3.4/8.9	Multiband features, decent bandwidth but moderate size
[14]	$0.28\lambda_0 \times 0.33\lambda_0$	2.10/2.91/4.32/ 5.83/7.88	43.4/- /50.0/162.73/ 279.50	1.36/−5.22/3.85/ 1.02/1.92	Multiband behavior but poor gain and large size
[20]	$0.64\lambda_0$ x $0.67\lambda_0$	3.55/5.35/6.1	350/750/250	3.9/3/5.9	Very large area
[25]	$0.18\lambda_0 \times 0.18\lambda_0$	1.42/2.43	20/120	3.63/7.80	Dual band functionality but less compact
[38]	$0.24\lambda_0 \times 0.15\lambda_0$	2.9/4.5/4.9/5.64	200/972/460	1.13 (max)	Compactness and multiband behavior but poor gain
[37]	$0.48\lambda_0 \times 0.29\lambda_0$	2.81/4.43/5.96/ 9.38	800/6700	4.65 (max)	Adorable gain and bandwidth but large area
[39]	$0.36\lambda_0 \times 0.36\lambda_0$	2.20/3.49/6.00	1200/220/810	1.33/0.95/2.78	Superior bandwidth but large size and poor gain
[40]	$0.33\lambda_0 \times 0.33\lambda_0$	2.5/5.2	690/1060	0.85/3.15	Dual band features, good bandwidth but large size
Realized DSSFA	$0.21\lambda_0 \times 0.26\lambda_0$	**2.43/3.61/4.20/ 7.71/8.69/12.90/14.41**	**170/280/320/4 20/200/760/> 930**	**13.14/6.54/6.03/ 4.67/3.83/6.87/ 10.39**	**Compactness with multiple resonances, appreciable gain and bandwidth**

absorbing material has been utilized during the measurement process. Figure 15 reveals the comparison of experimentally extracted and software generated radiation patterns at six chosen resonant points. It is worth noting that at the claimed lower resonant points (2.43, 4.20, and 7.71 GHz), partially deformed omnidirectional patterns are examined, as depicted in Fig. 15(a–c). However, for higher resonant points (8.69, 12.90, and 14.41 GHz), generation of higher order modes causes the appearance of deformed butterfly (arbitrary bidirectional) patterns (portrayed in Fig. 15d–f). Gain computation at each resonance is done by applying the Friis transmission formula. Figure 16 portrays the simulated and practically revealed gain and efficiency values associated with the Realized

https://doi.org/10.1017/S1759078726103122 Published online by Cambridge University Press

DSSFA. The presented figure reports that the Realized DSSFA gives an experimental gain of 8.25, 5.16, 5.47, 4.08, 3.35, 5.56, and 8.49 dB at the targeted frequency points (2.48, 3.58, 4.25, 7.65, 8.74, 11.83, and 14.44 GHz), respectively. It can be conferred that the computed gain values are highly remarkable. Similarly, the described structure produces experimental efficiency of 86.26%, 90.47%, 83.75%, 69.19%, 69.37%, 93.18%, and 87.16% at the above-said frequency points. Here, it is recognized that the experimentally extracted gain and efficiency values are found close to the software computed outcomes. At last, all the examined performance metrics (simulated and measured) associated with the Realized DSSFA are compiled in Table 9. Based on all these outcomes, it can be undoubtedly stated that the manufactured model with notable features exhibits compactness, multifunctionality, bandwidth as well as high gain and efficiency.

Comparison of realized DSSFA with certain prior reported antennas

A comprehensive comparison of the Realized DSSFA with certain prior reported antennas is tabulated in Table 10, for more limpidity. After critically examining all the values, it is noted that the Antennas reported in [12, 14], and [37] offered multiband functionality and decent bandwidth values but they possessed large volume. Antennas introduced in [2, 38, 39], and [40] exhibited large bandwidth values corresponding to the fundamental operational bands but they produced poor gain values in comparison to the Realized DSSFA. Furthermore, the designs described in [3, 10], and [20] claimed triple band functionality with adorable gain response but they showed less compactness. The designs mentioned in [7], and [25] followed dual band behavior and appreciable gain at the associated band but their physical dimensions were large. Therefore, based on the conducted comparative analysis, it can be anticipated that the Realized DSSFA demonstrates compactness, decent gain and functionality for multistandard wireless applications. This proves the recommended design's efficacy.

Conclusion

A novel, less complex, high gain HSA-ANN Ensembled hybrid approach based modified dual staircase-shaped multiband fractal antenna of remarkably small dimensions $26 \times 32 \times 1.6$ mm^3 is demonstrated in this paper. The formulated integrated algorithm helps in achieving the critical (pre-specified) frequency bands. Computational analysis validates that the developed ANN Ensembled models offer better values of performance assessment measures than the distinct ANN models. The experimentally analyzed prototype shows resonance at 2.48, 3.58, 4.25, 7.65, 8.74, 11.83, and 14.44 GHz with S11 of −15.54, −21.60, −14.72, −15.11, −13.99, −11.12, and −34.11 dB, respectively. At all the claimed frequency points, the demonstrated design gives adorable gain and efficiency. Moreover, antenna miniaturization of 33% is achieved with this optimal design. Based on Section 5, it has been undoubtedly stated that the Realized DSSFA is a promising candidate for numerous multistandard wireless applications.

Data availability statement. The authors confirm that the data supporting the findings of this research are available within the article. Raw data that support the findings of this research are available from the corresponding author, upon reasonable request.

Funding statement. Authors have not taken any funding from any institution or organization for completing this research. So, nothing is to declare.

Competing interests. The authors declare that they have no conflict of interest.

References

1. **Sharma N and Bhatia SS** (2021) Design of antenna by amalgamating staircase and hexagonal ring-shaped structures with the modified ground plane for multi-standard wireless applications. *Journal of Electromagnetic Waves and Applications* **36**(9), 893–911.
2. **Wang Z-G, You R, Yang M, Zhou J and Wang M** (2024) Design of a monopole antenna for WiFi-UWB based on characteristic mode theory. *Progress In Electromagnetics Research M* **125**, 107–116.
3. **Sran SS and Sivia JS** (2020) ANN and IFS based wearable hybrid fractal antenna with DGS for S, C and X band application. *International Journal of Electronics and Communications* **127**, ArticleId153425.
4. **Prasad N, Pardhasaradhi P, Madhav BTP, Isalm T, Das S and Ghzaoui ME** (2023) Radiation performance improvement of a staircase shaped dual band printed antenna with a Frequency Selective Surface (FSS) for wireless communication applications. *Progress In Electromagnetics Research C* **137**, 53–64.
5. **Ahmad Z, Kabir A and Bukhari SSH** (2021) A novel compact stair-shaped multiband fractal antenna for wireless communication systems. *Journal of Electrical Engineering* **72**(5), 306–314.
6. **Islam T, Ali EM, Awan WA, Alzaidi MS, Alghamdi TAH and Alathbah M** (2024) A parasitic patch loaded staircase shaped UWB MIMO Antenna having notch band for WBAN applications. *Heliyon* **10**(1), e23711. https://doi.org/10.1016/j.heliyon.2023.e23711.
7. **Kaur M and Sivia JS** (2019) Giuseppe Peano and Cantor set fractals based miniaturized hybrid fractal antenna for biomedical applications using artificial neural network and firefly algorithm. *International Journal of RF and Microwave Computer-Aided Engineering* **30**(1), 1–11.
8. **Das S, Mitra D and Chaudhuri SRB** (2019) Staircase fractal loaded microstrip patch antenna for super wide band operation. *Progress In Electromagnetics Research C* **95**, 183–194.
9. **Mark R, Mishra N, Mandal K, Sarkar PP and Das S** (2018) Hexagonal ring fractal antenna with dumb bell shaped defected ground structure for multiband wireless applications. *International Journal of Electronics and Communications* **94**, 42–50.
10. **Kaur A and Malik PK** (2021) multiband elliptical patch fractal and defected ground structures microstrip patch antenna for wireless applications. *Progress In Electromagnetics Research B* **91**, 157–173. https://doi.org/10.2528/PIERB20102704.
11. **Mezaal YS, Eyyuboglu HT and Ali JK** (2014) Wide bandpass and narrow bandstop microstrip filters based on Hilbert fractal geometry: Design and simulation results. *PLOS ONE* **9**(12), e115412. https://doi.org/10.1371/journal.pone.0115412.
12. **Jindal S, Sivia JS and Bindra HS** (2019) Hybrid fractal antenna using meander and Minkowski curves for wireless applications. *Wireless Personal Communications* **109**(4), 1471–1490. https://doi.org/10.1007/s11277-019-06622-5.
13. **Jain C and Singh S** (2019) Feed point optimization of Koch-Minkowski hybrid boundary antenna for ISM Band. *Wireless Personal Communications* **108**(4), 2403–2414. https://doi.org/10.1007/s11277-019-06528-2.
14. **Akkole S and Vasudevan N** (2021) Microstrip fractal multiband antenna design and optimization by using DGS technique for wireless communication. *Proceedings of the 6th International Conference on Inventive Computation Technologies (ICICT)*, Coimbatore, India, Jan 2021, pp. 72–77.
15. **Raj A, Dhubkarya DC, Srivastava DK and Mandal D** (2023) Design and analysis of square shape slot cut high gain Sierpinski carpet fractal antenna for wireless applications. *Microwave and Optical Technology Letters* **65**(8), 2337–2343. https://doi.org/10.1002/mop.33687.
16. **Sharma N, Sharma V and Bhatia SS** (2018) A novel hybrid fractal antenna for wireless applications. *Progress In Electromagnetics Research M* **73**, 25–35. https://doi.org/10.2528/PIERM18052403.
17. **Singh G, Kumar A, Singh MJ and Singh AP** (2024) Modified pentagonal fractal antenna for ultra-wideband applications in communication

https://doi.org/10.1017/S1759078726103122 Published online by Cambridge University Press

systems. *International Journal of Electronics Letters* **12**(4), 413–421. https://doi.org/10.1080/21681724.2024.2327091.
18. **Shandal SA, Mezaal YS, Mosleh MF and Kadim MA** (2018) Miniaturized wideband microstrip antenna for recent wireless applications. *Advanced Electromagnetics* **7**(5), 7–13. https://doi.org/10.7716/aem.v7i5.806.
19. **Siddiqui MG, Devesh AKS and Ansari J** (2018) Multi-band fractaled triangular microstrip antenna for wireless applications. *Progress In Electromagnetics Research M* **65**, 51–60.
20. **Kumari S, Awasthi YK and Bansal D** (2022) Proposed multiband fractal monopole antenna for WLAN and WiMAX applications. *Progress In Electromagnetics Research C* **127**, 239–249.
21. **Karanam R and Kakkar D** (2022) Artificial neural network optimized ultra wide band fractal antenna for vehicular communication applications. *Transactions on Emerging Telecommunications Technologies* **33**(12), e4620.
22. **Marzouk M, Nejdi IH, Youssef R, Barua S, Mohamed S, Ahmad S and Husseina M** (2024) Efficient broadband fractal antenna for WiMAX and WLAN. *Heliyon* **10**(5), e26087. https://doi.org/10.1016/j.heliyon.2024.e26087.
23. **Sran SS and Sivia JS** (2021) PSO and IFS techniques for the design of wearable hybrid fractal antenna. *International Journal of Electronics* **108**(12), 2039–2057.
24. **Dhaliwal BS, Kaur G, Kaur S and Pattnaik S** (2020) Low-cost fractal MIMO antenna design for ISM band using ANN. In S.Jain, M.Sood and S.Paul (eds), *Advances in Computational Intelligence Techniques*. Singapore: Springer, pp. 219–226.
25. **Kaur M and Sivia JS** (2019) ANN-based design of hybrid fractal antenna for biomedical applications. *International Journal of Electronics* **106**(8), 1184–1199. https://doi.org/10.1080/00207217.2019.1582712.
26. **Rajapriya S and Daniel RS** (2024) Artificial neural network-based multiband μ-negative Hilbert curve fractal antenna using RSRR unit cell. *Telecommunication Systems* **86**, 189–200.
27. **Kaur M, Krishan R, Kaur N and Sivia JS** (2024) Invasive weed optimization based compact hybridized fractal antenna design for RF energy harvesting and multifunctional wireless applications. *International Journal of Electronics and Communications* **184**.
28. **Mohammed YA and Naji DK** (2023) Sidelobe suppression of antenna array using harmony search algorithm. In *2023 IEEE 12th International Conference on Communication Systems and Network Technologies (CSNT)*, Bhopal, India, pp. 86–90.
29. **Guney K and Onay M** (2011) Optimal synthesis of linear antenna arrays using a harmony search algorithm. *Expert Systems with Applications* **38**(12), 15455–15462.
30. **Dhaliwal BS and Pattnaik SS** (2016) Performance comparison of bio-inspired optimization algorithms for Sierpinski gasket fractal antenna design. *Neural Computing and Applications* **27**(3), 585–592.
31. **Dhaliwal BS and Pattnaik SS** (2017) BFO-ANN ensemble hybrid algorithm to design compact fractal antenna for rectenna system. *International Journal on Neural Computing and Applications* **28**(1), 917–928. https://doi.org/10.1007/s00521-016-2402-9.
32. **Haque MA, Rahman MA, Al-Bawri SS, Yusoff Z, Sharker AH, Abdulkawi WM, Saha D, Paul LC and Zakariya MA** (2023) Machine learning-based technique for gain and resonance prediction of mid band 5G yagi antenna. *Scientific Reports* **13**, 12590. https://doi.org/10.1038/s41598-023-39730-1.
33. **Dhaliwal BS and Pattnaik SS** (2017) Development of PSO-ANN ensemble hybrid algorithm and its application in compact crown circular fractal patch antenna design. *International Journal on Wireless Personal Communications* **96**(1), 135–152.
34. **Yang SH and Kiang JF** (2015) Optimization of sparse linear arrays using harmony search algorithms. *IEEE Transactions on Antennas and Propagation* **63**(11), 4732–4738. https://doi.org/10.1109/TAP.2015.2476518.
35. **Elmezughi MK, Salih O, Afullo TJ and Duffy KJ** (2023) Path loss modeling based on neural networks and ensemble method for future wireless networks. *Heliyon* **9**(9), e19685. https://doi.org/10.1016/j.heliyon.2023.e19685.
36. **Balanis CA** (2005) *Antenna Theory: Analysis and Design*, 3rd. London: John Wiley & Sons.
37. **Regulagadda NR and Kumari UVR** (2023) A multiband flexible wideband CPW wearable slot antenna for biomedical and IoT applications. *Progress In Electromagnetics Research C* **135**, 131–144. https://doi.org/10.2528/PIERC23052102.
38. **Zade PL and Khade SS** (2024) Miniaturized novel multi resonance monopole planar antenna with slots, slits, split ring resonator. *Progress In Electromagnetics Research C* **145**, 75–82. https://doi.org/10.2528/PIERC24051102.
39. **Salim AJ, Mohammed JK, Al-Saedi H and Ali JK** (2024) A proximity-fed multi-band printed antenna for wireless communication applications. *Progress In Electromagnetics Research C* **145**, 153–165. https://doi.org/10.2528/PIERC23122503.
40. **Yassen MT, Hussan MR, Hammas HA, Al-Saedi H and Ali JK** (2019) A dual-band printed antenna design based on annular koch snowflake slot structure. *Wireless Personal Communications* **104**(2), 649–662. https://doi.org/10.1007/s11277-018-6039-0.



Dr. Manpreet Kaur born in Malout, Punjab, India. She has received her B.Tech degree as well as M.Tech degree in Electronics and Communication Engineering from Punjab Technical University, Jalandhar. She has completed her Ph.D. in hybrid fractal antenna designing from Punjabi University, Patiala, Punjab, India. Presently, she is working as an Assistant Professor in Electronics and Communication Section at Yadavindra Department of Engineering, Off-Campus of Punjabi University, Patiala, Punjab, India. She has published more than 75 research papers in several International Journals and International and National Conferences. Her research interest lie in areas of Neural Networks, microstrip antenna, fractal antenna, and hybrid fractal antenna design.



Dr. Navneet Kaur born in Malout, Punjab, India. She has received her B.Tech degree in Electronics and Instrumentation Engineering from Punjab Technical University, Jalandhar. Moreover, she has received her M.Tech and Ph.D. degrees in Electronics and Communication Engineering from Punjabi University, Patiala, Punjab, India. Presently, she is a member (MIE), Institution of Engineers, India. She has published more than 35 research papers in several International Journals and International and National Conferences. Her research interest lie in areas of Neural Networks, metamaterials, metasurface, and fractal antenna design.



Dr. Jagtar Singh Sivia born in Bathinda, Punjab, in 1976. He received B.Tech degree from Punjab Technical University, Jalandhar, Punjab, in Electrical and Electronics Communication Engineering in 1999 and he had obtained his master degree from Punjab Technical University, Jalandher, in 2005. He had received his Ph.D. degree from Sant Longowal Institute of Engineeering and Technology, Longowal, Punjab. Currently, he is a professor in Electronics and Communication Section at Yadavindra Department of Engineering, Off-Campus of Punjabi University, Patiala, Punjab, India. He has published more than 80 papers in several International Journals and International and National Conferences. His main interests are in Neural Networks, Electromagnetic Waves, Genetic Algorithms, Antenna System Engineering. Currently, he is the chairman of Electronics and Telecommunication Engineering Division Board, The Institution of Engineers, India. Mr. Sivia is also a member of Indian Society of Technical Education and International Association of Engineers.

https://doi.org/10.1017/S1759078726103122 Published online by Cambridge University Press